PHYSICAL REVIEW B **69**, 144121 (2004)

Solid-liquid equilibria in nanoparticles of Pb-Bi alloys

W. A. Jesser,[1] R. Z. Shneck,[2] and W. W. Gile[1]
[1]*Department of Materials Science and Engineering, University of Virginia, Charlottesville, Virginia 22903, USA*
[2]*Department of Materials Engineering, Ben-Gurion University of the Negev, Beer Sheva 84105, P.O. Box 653, Israel*

(Received 3 December 2003; published 28 April 2004)

The melting behavior of isolated nanoparticles of Pb-Bi alloys was observed by hot stage transmission electron microscopy. Dark-field images acquired as a function of temperature permitted the melting behavior of individual nanoparticles to be characterized as a function of their composition and size. In this way, the experimental measurements could be used to find the temperature at which the onset of melting occurred and the temperature at which the transition from a liquid-solid two-phase particle to a complete liquid particle occurred. From these data, phase diagrams of individual, isolated nanoparticles were constructed as a function of the size of the nanoparticle. Several deviations from the melting behavior of bulk materials were observed. For particles of a given composition the melting temperature is lowered relative to the melting temperature of bulk material and the depression of temperature increases with the inverse of the particle radius. The liquid and solid phases follow melting paths that form liquidus and solidus *bands* on the temperature-composition phase diagram. The range of two-phase coexistence shrinks as the solute concentration decreases, and the liquidus and solidus bands finally coalesce into a single line at low solute concentrations in apparent violation of the Gibbs phase rule. Of particular interest is the observation that melting begins and ends abruptly as temperature is increased. Considering the isolated particle as a thermodynamic system in contact with a heat reservoir and a pressure reservoir, the conditions for two-phase equilibrium in the particles were calculated from the total internal energy of the particle and the reservoirs. The loci of parameters of the calculated minimum points of the total energy were compiled to calculate a phase diagram for alloy nanoparticles as a function of their size. This calculated diagram contains all of the special features observed experimentally and agrees quantitatively with the experimental measurements. These features should be sufficiently general to apply to other alloys. The quantitative conformance of the experimental with the calculated results is sensitive to the material properties, in particular to the composition dependence of the surface energy of the liquid.

DOI: 10.1103/PhysRevB.69.144121 PACS number(s): 81.30.Bx, 05.70.Np, 61.46.+w

I. INTRODUCTION

Much of the interest in nanostructured materials originates from the challenge to find materials with properties that are substantially different from those of the same materials in larger-scale forms. New dielectric (e.g., Ref. 1), ferromagnetic (e.g., Ref. 2), optic (e.g., Ref. 3), catalytic (e.g., Ref. 4), and other properties are indeed being realized. Of particular interest are nanoparticles that exist in new structures, metastable structures, or known structures extended beyond the composition or stability ranges of ordinary bulk materials. Many examples were recently described. These include normally crystalline alloys as amorphous ones (e.g., Ref. 5), icosahedral nanoparticles (e.g., Ref. 6), carbon as fullerenes, and other structures (e.g., Ref. 7). Many metastable phases were identified during solidification or crystallization of amorphous alloys (e.g., Ref. 8). Extended ranges of stability appear as increased solubility and liquid phase premelting of solids as will be described below. The sustained melting of solids in confined spaces was also observed.[9] Enhanced solubility was found in many alloys, e.g., in Fe-Ag (attributed to segregation to grain boundaries),[10] Ni-Ag,[11] Ni-Al,[12] and Al-Zr,[13] and of hydrogen in metals.[14] Synthesis of nanocrystalline materials often yields phases known to be stable at higher temperatures or pressures, e.g., cubic $BaTiO_3$,[15] monoclinic yttria,[16] tetragonal zirconia,[17] γ-alumina,[18] and titania as anastase.[19] Many of these observations have been successfully explained in the framework of classical thermodynamics. Some were attributed either to the large surface energy[18] or to the large hydrostatic pressure exerted by the surface stress,[16] or to significant surface segregation.[20] It is therefore highly desirable to have a consistent, general formulation of the thermodynamics of nanoparticles. It should provide a comprehensive description of the role of the various relevant variables, including the surface energy, surface stress, adsorption to surfaces, composition, curvature, pressure, shape, and size, in the equilibrium states or phase diagrams of nanoparticles. In this work we present the results of an experimental study of the solid-liquid equilibria of nanosized binary alloys of Pb-Bi and a careful thermodynamical analysis. The melting of isolated, spherical nanoparticles of Pb-Bi alloys was observed by *in situ* transmission electron microscopy (TEM) and modeled by adding surface terms to the bulk thermodynamic equations of binary alloys. A temperature-composition-size phase diagram is ultimately derived.

The precursor to the binary phase diagrams of nanoparticles was the determination of the depression of the melting point in nanoparticles of pure elements. Lord Kelvin realized that small isolated particles will melt at a reduced temperature relative to the melting temperature T_m of bulk materials. This is called premelting.[21] He predicted that the melting temperature will change by ΔT_m in proportion to the curvature $1/r$ of a spherical nanoparticle and the latent heat of melting ΔH_m, by the well known Gibbs-Thomson formula

$$\frac{\Delta H_m}{T_m}\Delta T_m=\frac{2\gamma^{\mathrm{sl}}\overline{V^s}}{r} \tag{1}$$

where the solid-liquid surface energy is γ^{sl}, and the atomic volume of the solid is $\overline{V^s}$. Premelting behavior was first demonstrated experimentally by Takagi,[22] who used hot stage transmission electron microscopy to observe the melting temperature of a collection of isolated small crystals of pure bismuth, lead, and tin. Melting was determined by the disappearance of the crystalline diffraction pattern. Her work was followed by several investigations using dark-field electron microscopy to determine the melting temperature of individual isolated nanoparticles of In,[23–25] Sn,[25–29] Bi,[25,30,31] Pb,[23,30,31] Al,[32] Ge,[32] Ag,[32] Au,[33] Cu,[32] and CdS.[34] In these studies the $1/r$ dependence was assessed although the exact relation between them remained ambiguous.[25,27,33,35–37]

Extending the studies of the melting behavior of one-component nanoparticles to that of binary alloys has been accomplished for simple eutectic systems in the Al-rich side of the Al-Cu diagram,[38] In-Pb,[39] Bi-Sn,[40] and several hypothetical systems.[41] In the present work we extend the studies to the more complicated binary system of Pb-Bi, where special features of the melting behavior of nanoparticle alloys were experimentally revealed. An explanation of the behavior based on a deliberate thermodynamic account of the surface properties of the nanoparticles is presented.

II. EXPERIMENTAL METHODS

The experimental apparatus utilized for this study was a dedicated Siemens 1A transmission electron microscope, the specimen chamber of which has been replaced by a specially designed vacuum chamber to allow *in situ* physical vapor deposition of metals on very thin substrate films supported in a specimen cartridge made of high-thermal-conductivity copper-beryllium alloy. It is inserted into a heater that utilizes electromagnetically self-canceling bifilament tantalum wire for its heat source. A Chromel-Alumel thermocouple junction was attached near the specimen and calibrated by the melting temperatures of thick films of the pure metals. The melting temperature of flat thin films was found to be reduced by only 1–2 °C below that of bulk material of similar composition. Electron beam heating was estimated by conducting heating experiments with the electron beam of the microscope off and comparing to ones with the beam on. Heating from the electron beam was found to be only a few degrees when the beam current was at its minimum setting.

Substrate films of thin amorphous carbon supported on 100-mesh copper grids were placed in the specimen cartridge for coevaporation of Bi and Pb to nucleate nanoparticles. The carbon substrates were baked at 300 °C for at least 12 h at a pressure of 10^{-4} Pa to remove contamination and cooled to the deposition temperature. Then Pb and Bi (of purity 99.99–99.999 %) were evaporated from separate, wire-wound baskets of Mo and W, respectively. A molybdenum sheet shutter between the substrate and metal sources was used while outgassing and stabilizing the rate of deposition. Then the shutter was opened and particles were produced by covapor deposition of Bi and Pb. The composition of the vapor and the particles was controlled by the temperatures of the source baskets. The temperature of the substrate during the deposition was 480–520 K. In this range most of the alloys are liquid; hence spherical isolated particles were obtained (Fig. 1).

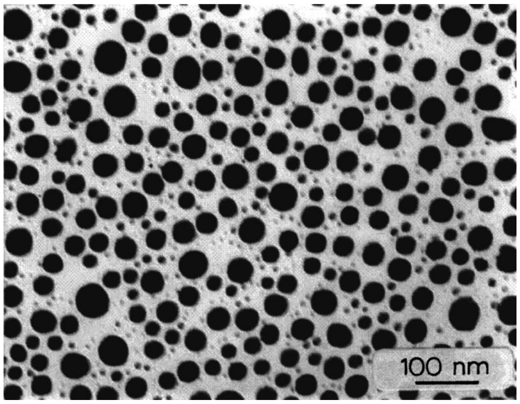

FIG. 1. Bright-field transmission electron micrograph of *in situ* deposited alloy particles of Bi-Pb. Compositions vary with size from 51 at. % Bi at a radius of 4 nm to 56 at. % Bi at a radius of 25 nm.

The individual nanoparticles are believed to be in a radiation equilibrium with the heater wall, whose temperature is measured by the thermocouple, because those particles in the radiation shadow of the grid bars melted at higher temperatures than their neighbors away from the grid bars. Radiation equilibrium allows particles of different sizes to be at the same temperature as the heater wall, so the measured temperature of the heater wall gives the temperature of the particle. If the nanoparticles were heated by conduction through the copper grid and the carbon substrate, different sized particles could be at different temperatures. Further, such a mode of heating would lead to the particles nearer the grid bar being at a higher temperature than those away from the grid bar, and hence the particles away from the grid bar would have to be heated to a higher wall temperature to melt. Since the opposite behavior was observed, a radiation thermal equilibrium rather than a mass thermal conduction mechanism is believed to be the operative mechanism of heating.

Melting experiments were performed by recording a series of dark-field micrographs while heating at a rate of 1 K/min. Selected area diffraction was performed in each specimen to determine the crystalline phases. Chemical energy-dispersive spectroscopy analysis was performed in a Philips EM 400 electron microscope on identical specimens, except that the particles were covered with a second layer of amorphous carbon to limit contamination. It was found that for a given deposition the size of a particle determined its composition. In order to detect the melting temperature of individual crystals, dark-field electron microscopy was applied. In this technique only electrons that were diffracted through a specific range of Bragg angles are used to create the image. Hence only crystals that have a selected orientation form bright images while other crystals have dark images. When a crystal melts the intensity of electrons diffracted through the specific angles is strongly reduced and

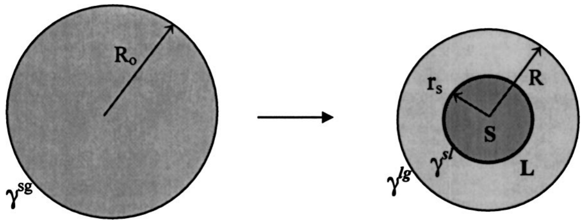

FIG. 2. The melting of a small solid particle of radius R_0 and surface energy γ^{sg} to form a solid core of radius r_s and interfacial energy γ^{sl}, completely wetted by its melt of surface energy γ^{lg} and thickness $R-r_s$.

the image of a particle that was bright becomes dark. Micrographs were taken at regular temperature intervals and were analyzed to obtain the melting temperatures versus particle size data for individual particles. For pure elements, the average temperature between the micrograph in which an individual particle still appears bright and the succeeding micrograph (only a degree or two higher) in which it appears dark is assigned as the melting temperature of that nanoparticle. For alloy nanoparticles the onset of melting appears as a reduction in the size of the bright region (in dark-field mode) corresponding to the sudden appearance of an amorphous (liquid) layer surrounding the crystalline core (two-phase solid-liquid equilibrium). This onset of melting is taken as the solidus temperature. Similarly, the temperature at which the same, two-phase (solid-liquid) nanoparticle transforms to complete liquid (the entire particle appears dark) is taken as the liquidus temperature. The temperature interval between these two melting events defines the range of temperatures over which the solid and liquid coexist in equilibrium.

III. EXPERIMENTAL RESULTS

Most of the particles in the Pb-Bi system were single phase and single grain and showed a spectrum of sizes and compositions after deposition. A typical TEM micrograph of as-deposited nanoparticles is shown in Fig. 1.

Upon heating, the initial melting of the particles was confirmed to take place by the formation of a definite amount of liquid sheath surrounding a crystalline core. This is consistent with the usual wetting condition of a melt in contact with its solid. Further heating of the liquid-solid particles showed shrinkage of their dark-field images, without a concomitant diminution in the size of their bright-field images, i.e., shrinkage of the crystalline solid. In some cases it was possible to discern a faint dark-field image of the peripheral edge of the liquid sheath, which had essentially the same size R_0 as that particle before any melting occurred.

At a specific temperature reached during heating, a liquid sheath of a definite thickness appears *suddenly* and forms a layer around the solid core. This is the first indication of melting. Simultaneously with the appearance of a liquid sheath the radius of the solid is observed to change abruptly from R_0 to a value between $0.95R_0$ and $0.8R_0$. This abrupt transition is schematically shown in Fig. 2.

After this abrupt melting the liquid layer *gradually* increased in thickness as the temperature increased. Then at a higher specific temperature the remaining solid core melts *suddenly* to form an entirely liquid particle. The solid core of radius ranging between approximately $0.8R_0$ and $0.7R_0$ thus abruptly disappears from the image. The solid core of many particles that show up bright in the dark-field image "blinks" on and off before the particles completely disappear. This is interpreted as an oscillation in the orientation of the particle in and out of the Bragg condition. As mentioned earlier, for each composition and size of an individual particle the temperature at which the liquid sheath first forms is designated as a solidus point. Similarly, the temperature at which the solid core of that particle completely melts is designated as a liquidus point.

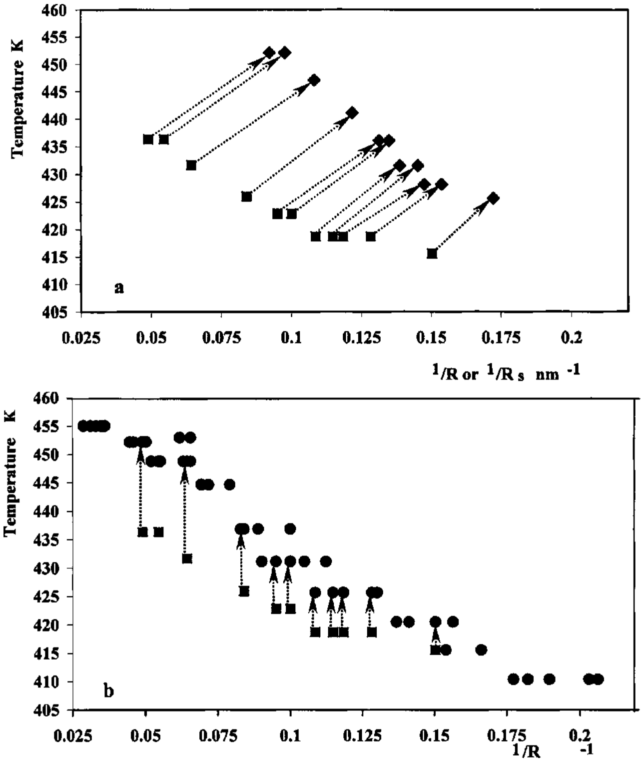

FIG. 3. The dependence of the solidus and liquids temperatures on the size of a set of nanoparticles. (a) Two points connected by thin arrows represent a single particle, which begins to melt abruptly at the lower temperature; then its solid core gradually shrinks until it reaches the size designated by a rhombus, where it abruptly melts. (b) The liquidus and solidus temperatures of a larger collection of particles. The composition of the particles resides in the ε-phase region varying with particle size from 51 at. % Bi for particles of 4 nm radius to 56 at. % Bi for 25 nm radius.

The melting behavior of individual particles obtained in a single deposition was determined as a function of their size and composition. Representative data are shown in Figs. 3(a) and 3(b), determined for compositions corresponding to the ε-phase field of the bulk diagram (51–56 at. % Bi). In Fig. 3(a) the (solidus) temperature at which melting begins for each particle of the indicated size R_0 is represented by a square and the (liquidus) temperature for which the solid-liquid abruptly transforms to complete liquid is denoted by a rhombus plotted at the solid core radius r_s. The pair of points for the same particle are connected by an arrow. In Fig. 3(b) the liquidus and solidus temperatures for a collection of individual particles are plotted against the full particle

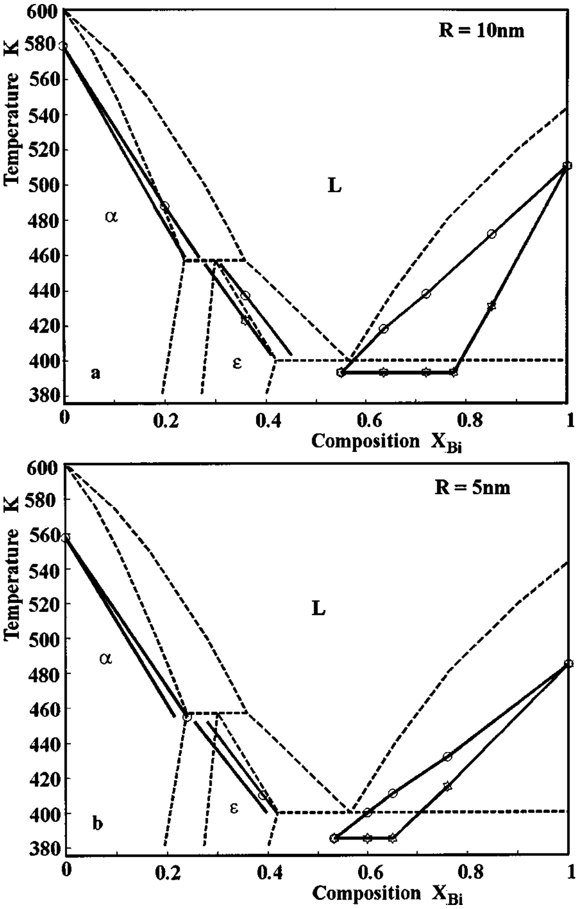

FIG. 4. The experimental binary phase diagram for Bi-Pb nanoparticles. The dashed lines are the bulk phase diagram and the solid lines interpolate the experimental observations into the phase diagram of the nanoparticles for particles of (a) 10 nm radii, (b) 5 nm radii. The symbols denote experimental data points: stars stand for the start of melting and circles for the end of melting.

radius R_0, by moving the rhombi of Fig. 3(a) from r_s to R_0 and adding several liquidus points for which no corresponding solidus point was determined. One can see that the points vary reasonably linearly with the inverse of particle radius. The slope of the solidus points is less than that for the liquidus points; hence at a particular size below about 7 nm the liquidus temperature and the solidus temperature merge into the same temperature. This corresponds to the disappearance of the solid-liquid two-phase equilibrium region.

Combining the data for the ε phase with that for the Pb-rich solid solution and the Bi-rich solid solution leads to the two phase diagrams for nanoparticles of 10 nm radius [Fig. 4(a)] and 5 nm radius [Fig. 4(b)]. From these figures one can see that the solidus composition and the corresponding solubility of Pb in Bi dramatically increased for nanoparticles, tenfold from its bulk value, which is only a few at. % of Pb in Bi. On the other hand, the solidus composition and solubility of Bi in Pb which in bulk form is significant (10–29 at. % Bi) changed only slightly. Also shown in these figures are the depression of the melting points and a substantial narrowing of the three solid-liquid fields showing that the coexistence of solid and liquid is becoming increasingly difficult as particle size is reduced to the nanoscale. For sufficiently small sizes of less than 5 nm radius one can expect the solid-liquid region of coexistence to disappear as was mentioned in the discussion of Fig. 3 and has been reported with the Sn-Bi system.[40]

The thermodynamic analysis of the equilibrium in the solid-liquid state depicted in Fig. 2 is presented in the Appendix. The details needed for the calculations are included in the next section.

IV. METHOD OF COMPUTATION

A. The thermodynamic formulation details

The states of equilibrium were found in two ways according to the analysis in the Appendix: (i) plotting of the thermodynamic potential $\Delta\phi$ [Eq. (A8)] as a function of the composition of the liquid phase, X^l, and the fractional amount of the liquid, f_l, and then searching on these surfaces for minima, and (ii) solving the analytical conditions for equilibrium [Eq. (A15)].

1. Plots of $\Delta\phi(f_l,X^l)$

Calculations of ϕ require it to be related to a reference state, which is naturally chosen to be the solid particle of the same overall composition X_0. Hence the following difference has been calculated, according to Eq. (A8):

$$\Delta\phi=\phi^{s+l}-\phi^{s}, \tag{2a}$$

representing the energy change upon transforming (melting) of a single solid particle into a two-phase state of a solid core enveloped by a liquid sheath (Fig. 2):

$$\begin{aligned}\Delta\phi(f_\ell X^\ell)=&\sum_i n_i^s\mu_i^s(0,X_i^s)+\sum_i n_i^l\mu_i^l(0,X_i^l)+\gamma^{\mathrm{sl}}\Sigma^{\mathrm{sl}}\\&+\gamma^{\mathrm{lg}}\Sigma^{\mathrm{lg}}+P^{\mathrm{ext}}(n^s\overline{V^s}+n^l\overline{V^l})-\Bigg(\sum_i n_i^t\mu_i^s(0,X_0)\\&+\gamma^{\mathrm{sg}}(X_0)\Sigma^{\mathrm{sg}}+P^{\mathrm{ext}}n^t\overline{V_0^s}\Bigg).\end{aligned} \tag{2b}$$

Here the chemical potentials are explicit functions of the pressure and composition. The number of moles of each constituent obeys the mass conservation equation (A12). ϕ is calculated and plotted as a function of the liquid composition X^l and the fraction of the liquid in the two-phase particle f_l.

The Gibbs free energy of mixing bulk liquid and solid solutions are ΔG_M^l and ΔG_M^s, respectively. The excess free energies of mixing are represented by the Redlich-Kister series taken from the Scientific Group Thermodata Europe (SGTE) database of[42] THERMOALC for each phase p:

$$\Delta G_M^{\mathrm{ex},p}=X_AX_B[L_0^p+L_1^p(X_A-X_B)+L_2^p(X_A-X_B)^2] \tag{3}$$

where the three coefficients L_i depend on temperature through the constants L_{i1} and L_{i2}:

$$L_i=L_{i1}+L_{i2}T. \tag{4}$$

The chemical potentials of each element are derived from Eq. (3) using known thermodynamic relations (e.g., Ref. 42)

TABLE I. Thermodynamic data for Bi-Pb solutions.

Property	Bi	Pb
γ^{sv} ($\mathrm{J\,m^{-2}}$)	0.404 (Ref. 44)	0.52 (Refs. 44, 52, 53)
$d\gamma^{\mathrm{sv}}/dT$ ($\mathrm{J\,m^{-2}\,K^{-1}}$)	-2.9×10^{-5} (Refs. 44, 54)	-1×10^{-4} (Refs. 44, 54)
γ^{sl} ($\mathrm{J\,m^{-2}}$)	0.065 (Ref. 44)	0.05 (Refs. 44, 55)
γ^{lv} ($\mathrm{J\,m^{-2}}$)	0.375 (Refs. 43, 56)	0.46 (Refs. 43, 52, 56)
$d\gamma^{\mathrm{lv}}/dT$ ($\mathrm{J\,m^{-2}\,K^{-1}}$)	-7×10^{-5} (Refs. 43, 52)	-2.6×10^{-3} (Refs. 43, 52)
γ_{lv} ($\mathrm{J\,m^{-2}}$)	$0.3755+0.0643X_{\mathrm{Pb}}+0.0099X_{\mathrm{Pb}}^2 -(7.1-6.2X_{\mathrm{Pb}}+6.6X_{\mathrm{Pb}}^2)\times10^{-5} \times(600-T)$ (Refs. 46, 47)	
V^l (10^{-6} $\mathrm{m^3\,mole^{-1}}$)	20.90 (Ref. 43)	19.58 (Ref. 43)
$\frac{1}{v}dV^l/dT$ (10^{-6} $\mathrm{K^{-1}}$)	110	127
V^s (10^{-6} $\mathrm{m^3\,mole^{-1}}$)	21.62	18.92
$\frac{1}{v}dV^s/dT$ (10^{-6} $\mathrm{K^{-1}}$)	40	87
T_{melt} (K)	544	600
ΔG_m from α phase (J/mole)	$2500-7.4T$	$4799-7.99T$ (Ref. 42)
ΔG_m from ε phase (J/mole)	$2100-7.4T$	$4474-8.948T$

	α phase (Ref. 33)	ε phase	Liquid phase
α_V (10^{-6} $\mathrm{m^3\,mole^{-1}}$)	[a]	[a]	0.24 (Ref. 51)
L_0 (J/mole) (Ref. 42)	$6993-22.33T$	$3897-22.88T$	$-980-10.75T$
L_1 (J/mole)	0	0	$-41+0.0071T$
L_2 (J/mole)	0	0	$960-0.46T$

[a] Taken as zero in the absence of data.

and substituted in Eq. (2b). Equation (3) for ΔG_M assumes that the components are already in the crystal structure of the resultant solution; when this is not the physical case a Gibbs free energy of transformation (“lattice stability” term) ΔG_{tr} is added to each component.

The surface energies of alloys depend on their composition. There is a large uncertainty in the values of surface energies of solid-liquid interfaces γ^{sl} of pure elements and therefore, of their alloys.[43,44] For the sake of simplicity a linear dependence was assumed between γ^{sl} of pure Pb and of pure Bi. On the other hand the surface energies of the liquid-gas surfaces γ^{lg} are reasonably well determined. We chose the method of Tanaka *et al.*[45] to calculate the variation of γ^{lg} with composition, using the surface energies of the pure elements and the Gibbs free energies of the constituents in bulk liquid solutions. The resulting function was then approximated by a polynomial given in Table I. This polynomial agrees well with direct measurements in the Pb-Bi system.[46,47] Here it is used also to calculate the adsorption to the liquid-gas surface Γ_i according to the Gibbs adsorption equation.[48] The convention defined by Kaufman and Whalen,[49] namely, that $\Gamma_i=-\Gamma_j$, for a binary alloy consisting of components i and j, was adopted to calculate the adsorption of each element by the relation

$$\Gamma_i=-X_j\frac{d\gamma}{d\mu_i}=-X_j\frac{d\gamma}{dX_i}\frac{dX_i}{d\mu_i}. \tag{5}$$

The Gibbs adsorption equation accounts for the whole excess quantity of material adsorbed to an unknown number of atomic layers at the surface. It also assumes the existence of an underling “bulk” reservoir of material, which is obviously unrealistic when the liquid sheath is thin. Hence the adsorption derived from Eq. (5) was modified to have a dependence on the thickness of the liquid sheath, h. A function was chosen to depress the adsorption of a thin layer and then to show a rapid increase to its full value [Eq. (5)] as h increases. The factor D by which Γ_i is reduced is

$$D=\frac{2+\sqrt[4]{h/R_0}}{3}. \tag{6}$$

Thereby $\Gamma_i(h)=-DX_j\partial\gamma/\partial\mu_i$ was used in Eq. (A8) for ϕ [in the second approach to finding the equilibrium states by solving Eqs. (A15), D is introduced by the equation of mass conservation]. This feature of the adsorption seems physically reasonable but it is open to question. Fortunately, ϕ is not sensitive to the form of D.

It has been argued that the surface energy varies with curvature. This effect was analyzed by Koenig,[50] who derived the relation between γ and the curvature. From the result the relation of the adsorption and the curvature can also be derived. Application of these results shows that they have an influence of about 20% on Γ but only about 0.5% on γ and therefore a small effect on the equilibrium states. Accordingly, this effect will not be included in the present calculations.

The particle is assumed to be a solid sphere surrounded by a concentric spherical shell of liquid so that the following geometrical relations hold:

$$\Sigma^{\mathrm{sl}}=4\pi r^2,\quad \Sigma^{\mathrm{lv}}=4\pi R^2,\quad V^s=\frac{4\pi r^3}{3},$$

$$V^l=\frac{4\pi}{3}(R^3-r^3). \tag{7}$$

For lead and bismuth the partial molar volumes in a solution are nearly equal to those of the pure elements.[43] Thus the molar volume of the solid alloy $\overline{V^s}$ is taken to be a weighted average of the molar volumes of the pure solid elements $\overline{V}_i^0$:[43]

$$\overline{V^s}=X_A^s\overline{V}_A^{0s}+X_B^s\overline{V}_B^{0s}. \tag{8}$$

Available data on the molar volume of the liquid alloys were fitted to a parabolic law:[51]

$$\overline{V^l}=X_A^l\overline{V}_A^{0l}+X_B^s\overline{V}_B^{0l}+\alpha_V X_A^l X_B^l, \tag{9}$$

where α_V is a regular solution parameter. The specific volumes of the liquid and solid elements are assumed to be linear functions of the temperature:

$$\overline{V}=V_i^0+\alpha_T T, \tag{10}$$

where α_T is the thermal expansion coefficient.

The computation proceeds as follows. The fraction of liquid in the two-phase particle, f_l, and the liquid composition X^l are picked in a regular array. The adsorption to the s-l surface is calculated from X^l. The composition of the solid is now determined by solving the mass conservation equation (A12). This allows determination of the volumes and the bulk Gibbs free energies of mixing of the two phases and the areas and surface energies of the two interfaces. Then $\Delta\phi$ is calculated by summing the terms in Eq. (A8)

2. Solution of the equilibrium condition

The set of two equilibrium equations (A15) and an equation for the mass conservation of one component (A12) are numerically solved so that they are satisfied for a chosen overall composition X_0. The details of the required terms are given in Sec. IV A 1. The equations have a second solution as well as the desired one. One can distinguish the desired solution by plotting $\Delta\phi$ and confirming that the solution corresponds to the minimum energy. The second solution is a saddle point maximum.

B. Thermodynamic data

The thermodynamic data used for the calculations of the Pb-Bi system are listed in Table I.

V. RESULTS OF THE CALCULATIONS

In this section the thermodynamic model developed in the Appendix and evaluated by the computational method discussed in Sec. IV will be compared to the experimental data presented in Sec. III. This comparison takes the form of calculating temperature-composition phase diagrams for isolated nanoparticles of radii 10 and 5 nm, which are the same radii reported in the experimental results Sec. III. The *in situ* TEM measurements in a hot stage provided not only the temperature-composition region over which the solid and liquid phases coexist but also the qualitative melting behavior, namely, an abrupt onset of melting and an abrupt final melting. The thermodynamic model will also be evaluated with regard to this melting behavior. In the Appendix and in Sec. IV, two equivalent approaches were outlined. One is to evaluate the location of minima in the three-dimensional (3D) plot of $\Delta\phi$ versus composition of the liquid and the fraction of the system which is liquid. The other is to solve the analytical conditions for the equilibrium state of the system. The two methods yield essentially identical results.

A. Terminal solid solutions

The Bi-rich solution in the Pb-Bi phase diagram shows very limited solubility in the bulk. The thermodynamic description of such phases is usually arbitrary. It is typically taken as a regular solution with large positive interaction parameter L_0 which reproduces the small solubility. This parameter is not reliable for extension beyond the limited solubility range and hence no calculation will be performed for this side of the phase diagram. Tanaka and Hara[41] concluded that experimental observations of nanoparticles of such solutions with low solubility can reveal the hidden part of ΔG_{mix}.

On the other hand, the solubility in the Pb-rich terminal solution is relatively large and the existing thermodynamic description of these phases is more reliable. Therefore detailed calculations were undertaken on this side of the diagram. We chose to illustrate the model calculations for a nanoparticle of radius 10 nm and overall composition 0.2 Bi by plotting $\Delta\phi$ and searching for minima over a range of temperatures. Two types of plots are useful for following the trends of the equilibrium states as a function of temperature. One is the 3D $\Delta\phi$ energy plot and the other is its projection on a 2D contour map. The 3D $\Delta\phi$ energy surface is shown in Fig. 5(a) at a temperature for which an energy minimum exists. The appearance of a minimum on the energy surface indicates the existence of a stable solid-liquid equilibrium, i.e., a two-phase region on the phase diagram. To better see the location of the minimum an enlarged view is given in Fig. 5(b). The minimum is a shallow one lying in a long, slightly curved, energy valley running almost parallel to the axis of liquid fraction. As temperature increases the position of the elongated valley gradually moves while the location of the relative minimum slides along the valley toward larger fractions of liquid. These trends of the energy valley and its shallow minima can be accurately followed on 2D contour plots.

A set of four contour plots of $\Delta\phi$ is shown in Fig. 6 drawn for the same parameters as Fig. 5 for four different temperatures.[70] Figures 6(a) and 6(b) are drawn for two nearly equal temperatures, one at a temperature (468.5 K) for which the relative minimum does not exist and the nanoparticle has its lowest energy when it is completely solid, and the second for a temperature (469 K) at which the relative minimum first appears. The significant features are that in

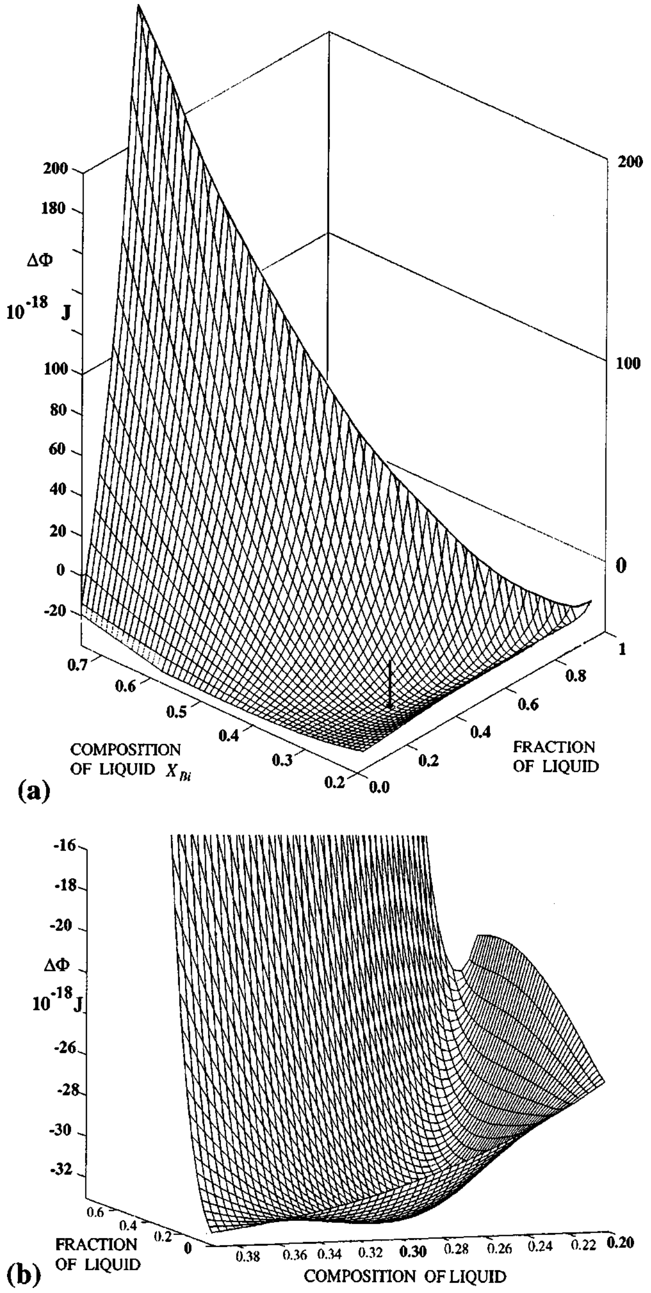

FIG. 5. 3D plots of $\Delta\phi$ at 475 K for a particle of radius 10 nm and nominal composition 0.2 Br. (a) General view; the location of the shallow minimum is indicated by a vertical arrow. (b) A close up viewed from the left side of (a).

Fig. 6(a) the energy valley exists but it is monotonically inclined so that the solid is the stable phase, while in Fig. 6(b) the energy valley first drops δ to the relative minimum and then rises to the 100% liquid point. Accordingly, 469 K is the first temperature at which the two-phase solid-liquid equilibrium appears. Notice that, unlike the bulk case for which an infinitesimal amount of liquid can be in equilibrium with the solid, here a finite amount of liquid is required for the first equilibrium, namely, the liquid sheath is expected to appear abruptly with a finite thickness when the temperature reaches the solidus temperature. A consequence of this discontinuous transition from all solid to a finite amount of liquid coexisting with the solid core is that the composition of the equilibrium solid will also jump discontinuously from its initial value of 0.2 Bi to another value. Recently Shirinyan and Gusak analyzed a phase diagram of nanoparticle alloys with a stoichiometric compound and found a temperature range for which an abrupt transformation occurs.^{71} The origin of the abrupt transformation in their work and this work is similar and derives from the variation in energy with size and composition.

The presence of an abrupt initial melting in the model agrees with experimental observation. Once the relative minimum appears, further increases in temperature lead to its sliding along the energy valley toward larger amounts of liquid. Accompanying this motion along the valley is the tilting of the valley toward the 100% liquid point, i.e., the end of the valley at high fractions of solid becomes higher in energy while the end of the valley at high liquid fraction becomes lower. Interestingly, at some elevated temperature the energy of the state of 100% liquid energy can be *lower* than the energy of the relative minimum. At such temperatures a saddle point maximum exists between the relative minimum and the absolute minimum at 100% liquid. Even though a lower-energy state is available to the system for 100% liquid, complete melting is suppressed by the inability of the system to jump over the saddle point. Further increase in temperature causes both the maximum and the relative minimum to disappear leading to the two-phase solid-liquid equilibrium being replaced by 100% liquid. This transition is illustrated in Figs. 6(c) and 6(d). As the temperature is increased from 493 to 493.5 K the relative minimum disappears, representing an abrupt disappearance of the solid core at the liquidus temperature. This is in agreement with the experiment. The compositions of the phases should discontinuously jump at the liquidus temperature 493.5 K, i.e., the liquid composition abruptly changes from about 0.23 bismuth to the overall composition of the particle, 0.20 bismuth. The result of the analysis is that a nanoparticle of average composition 0.2 bismuth and radius 10 nm shows two abrupt meltings, one at the solidus temperature of 469 K and another at the liquidus temperature of 493.5 K. Between these two temperatures a two-phase equilibrium exists. By selecting other initial compositions and applying similar calculations, the temperature dependence of the liquidus and solidus temperatures can be determined and hence the phase diagram for a nanoparticle of radius 10 nm can be drawn. Before performing these calculations, it is helpful to explore the compositions of each of the two phases in the temperature range between 469 and 493.5 K.

For *bulk* phases in a two-phase region of a binary phase diagram, the equilibrium compositions of the phases are given by the ends of the tie lines lying on the liquidus and solidus lines. However, because of the abrupt initial melting and final melting, the liquidus and solidus lines no longer give the compositions of the actual phases. To explore this further it is instructive to plot the compositions of the two phases coexisting in equilibrium as the temperature is increased. Upon reaching the solidus temperature the first amount of liquid appears with a composition X^l greater than

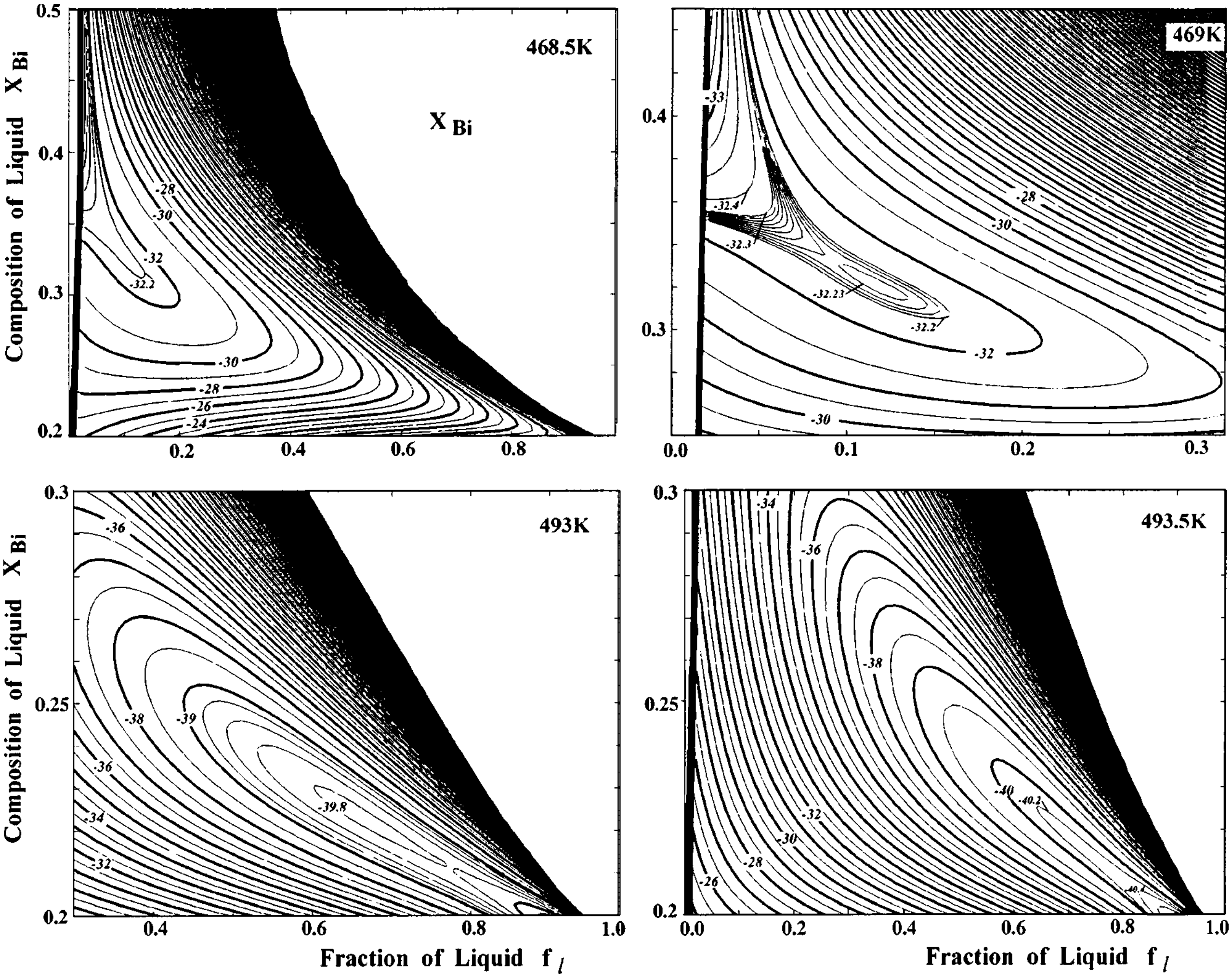

FIG. 6. Contour maps of $\Delta\phi$ at four temperatures, following the melting path of a particle of radius 10 nm and nominal composition 0.2 Bi. The abrupt initiation of melting and the abrupt end of melting, emphasized by the choice of the four temperatures, take place within small temperature intervals. Notice that equienergy lines with finer spacings were drawn in the vicinity of the minima. Units are 10^{-18} J per particle.

the initial composition of the particle X_0. Mass conservation coupled with the feature that the amount of first-to-form liquid is substantial places the composition of the solid phase at a significantly smaller bismuth amount than 20%. This is shown in Fig. 7 as a discontinuous jump in the composition of the solid from $X_0 = 0.2$ bismuth to about 0.17 bismuth. As temperature is increased the amount of liquid increases; the compositions of the solid and liquid follow their respective paths. These paths always lie *outside* the two-phase region bounded by the liquidus and solidus lines and exhibit a different temperature dependence from that of the liquidus and solidus lines. The composition lines permit determination of the composition of the phases and serve for application of the lever rule for mass conservation. A tie line has been drawn at 470 K in Fig. 7. Note that it does not have its ends on the liquidus and solidus lines, but runs outside these to the compositions of the phases, as it must for mass conservation.

In order to determine the phase diagram for this nanoparticle of radius 10 nm, a series of initial compositions is analyzed in the same way. A particle with similar initial size but different composition will melt at a different temperature. Hence the radius of the solid core will be different for the two particles when they reach the same temperature. Therefore particles of different composition will follow different melting paths. These shallow “s” melting paths for the compositions of coexisting solid and liquid will have loci that map into composition *bands* (Fig. 7). These solidus and liquidus bands show where the ends of the tie lines lie and have boundaries indicating states of the start and end of melting, respectively. The liquidus and solidus lines define the part of the phase diagram in which two-phase equilibrium exists.

When the positions of the liquidus and solidus lines on the nanoparticle phase diagram are quantitatively compared to their counterparts on the bulk phase diagram, one finds that the two-phase field is considerably narrower and shifted to lower temperatures. Such a comparison will be made later in this section and can be seen in Fig. 4.

B. Intermediate solid solution (ε phase)

The intermediate phase of Pb-Bi shows the same type of behavior as that of the terminal solid solutions, namely,

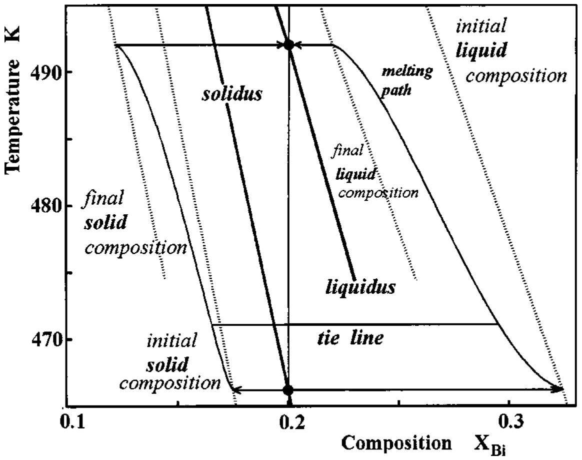

FIG. 7. The process of melting of the 10 nm particle with nominal composition 0.2 Bi plotted in the *T-X* plane.

abrupt melting, narrowed two-phase field, and shifts of the liquidus and solidus lines to lower temperatures. A feature of both the ε phase and the Pb-rich phase that was not discussed in detail in the preceding subsection is the narrowing of the two-phase field as the initial composition X_0 is decreased. Consider a series of initial compositions from $X_0 = 0.4$ bismuth decreasing to 0.25 bismuth, corresponding to the ε phase and 10 nm radius. From the solidus temperature for which the first melting of the ε phase occurs in the case of 0.4 bismuth, to the liquidus temperature where the final melting occurs, the fraction of liquid begins at about 0.16 and ranges up to about 0.55. When the initial composition of 0.3 bismuth is investigated the fraction of liquid that appears at the solidus temperature is about 0.17 and it ranges up to 0.35 at the liquidus temperature. This narrowing of the range of liquid fractions with initial composition is plotted in Fig. 8(a) for four values of X_0. The noteworthy feature here is that for $X_0 = 0.25$ the range of liquid fractions reduces to zero, represented by a single point. At this point the liquidus line merges with the solidus line and the range of the two-phase field narrows to a single line. Melting for this initial composition begins and ends at a single temperature. This is the same behavior found in a pure bulk solid. For comparison, the fraction of liquid range for the Pb-rich phase is also shown where it is seen that when X_0 becomes 0.06 bismuth, the two-phase field disappears and complete melting occurs at a single temperature.

C. Three-phase equilibrium

The coexistence of a liquid with two solid phases appears in the Pb-Bi system in bulk form at a peritectic temperature and again at a eutectic temperature. The three-phase equilibrium was not investigated experimentally, nor was it analyzed with the thermodynamic model. Because of the heterogeneous pressure in the system and its dependence on the amounts of the phases present through the surface curvature, one can expect the three-phase region of the bulk diagram to span a temperature range. Investigation of the three-phase equilibria is left for a future work.

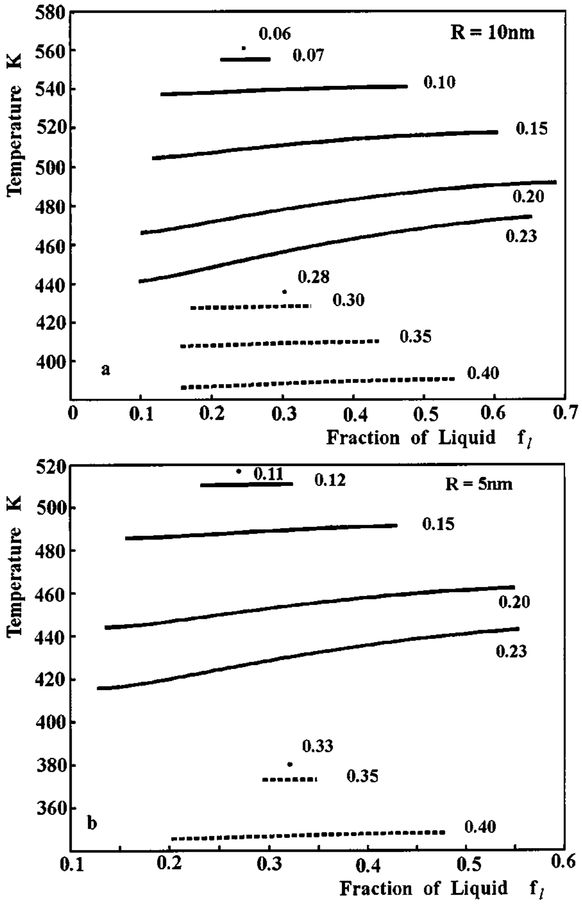

FIG. 8. The evolution of the amount of liquid during heating of (a) 10 (b) 5 nm radius particles of several nominal compositions. Compositions in the α range are plotted by solid lines; compositions in the ε range are plotted by broken lines.

D. Size-dependent phase diagram

From the information in the above subsections, one can construct a 3D phase diagram for nanoparticles with reciprocal size being the third axis. The experimental determination of the phase diagram has already been performed and is shown in Fig. 4 for two particle radii, 10 and 5 nm. Here the thermodynamic model is used to calculate the liquid equilibrium with the Pb-rich phase and the ε phase. The Bi-rich side of the phase diagram for these two sizes was not modeled as explained in Sec. V A. Two *T-X* diagrams are stacked on a reciprocal radius axis. The result is displayed as a perspective drawing in Fig. 9. Included in each 2D section and shown by light dashed lines is the projection of the bulk phase diagram which normally would be located at the $1/R = 0$ position. The liquidus and solidus lines and bands are included in the diagram. The bands are composed of pairs of composition paths for the coexisting solid-liquid. The agreement between the model and the measurements is believed to be satisfactory.

Several features of the phase diagram for Pb-Bi nanoparticles are apparent from Fig. 9. The melting points of the pure elements have been depressed by more than 20 K at $R = 10$ nm and about 45 K at $R = 5$ nm. The temperatures over which two phases (liquid and solid) coexist have been

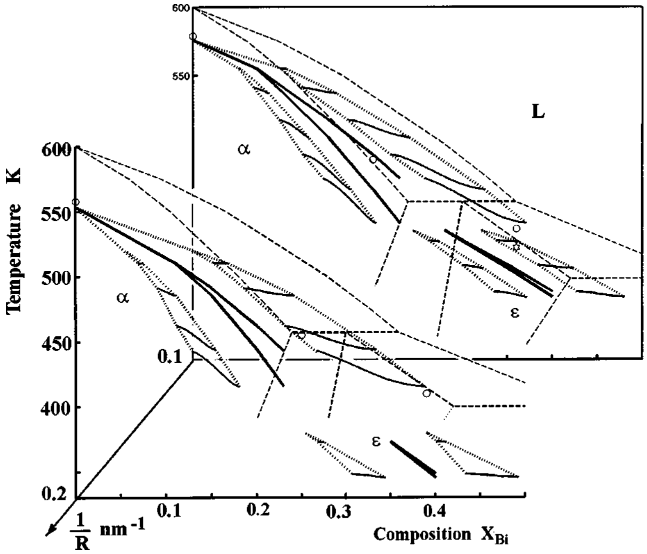

FIG. 9. The calculated Pb-Bi phase diagram of isolated nanoparticles for 10 and 5 nm radii are stacked to make a composite phase diagram as a function of the particle size. The bulk phase diagram is plotted in dashed lines. The liquidus and solidus are drawn as thick lines; the actual compositions of the liquid and solid at the beginning and ending of melting are drawn as broken lines. The actual paths of melting of the solid and the liquid are shown in thin continuous lines. The experimental data are represented by circles and stars.

depressed from their bulk values and the temperature field has also been considerably narrowed. For all of the single-phase regions, it is found that the solidus lines have been shifted toward the lead-rich side of the phase diagram as compared to the bulk case. This corresponds to an increase in lead solubility of bismuth in the liquid and a decreased solubility in the solid (shown in Fig. 4). On the other hand, the increase in lead solubility in the Bi-rich solid phase is dramatic in the nanoparticle when compared to the small solubility found in the bulk alloy. Perhaps the most interesting feature of this diagram is the merging of liquidus and solidus lines and bands, resulting in the pinching off of the two-phase regions. Above this pinching-off temperature there is no longer a stable equilibrium between liquid and solid phases. The equilibrium becomes an unstable one so the particle is experimentally found as either all liquid or all solid. The size dependence of these features clearly shows an increased effect of all the features discussed as size decreases, namely, an increased depression of the melting points and two-phase fields; increased narrowing of the two-phase fields such that below some size they may disappear altogether; narrowing of the solidus and liquidus bands; and change of the solubility in the single phases.

VI. SUMMARY AND CONCLUDING COMMENTS

In this paper it is shown that equilibrium phase diagrams for isolated nanoparticles are significantly different from those of bulk alloys. Measurements for the Pb-Bi alloy from *in-situ* TEM experiments on isolated nanoparticles of radii ranging from 5 to 40 nm have been compared to a model developed from thermodynamic first principles. Agreement between the model and experiments is quantitatively reasonable and qualitatively accurate, e.g., in describing the abrupt melting phenomena. Phase diagrams for nanoparticles are affected by the presence of curved surfaces that shift the chemical potentials and internal pressures from their values when in bulk form. The features of the phase diagram for nanoparticles that emerge as significantly different from that of bulk phases are as follows. (i) There is a size-dependent melting temperature depressed from the values of bulk material. (ii) There is a narrowing of two-phase fields to the degree of pinching off to a line. (iii) The conventional liquidus and solidus lines are replaced with shifted liquidus and solidus lines lying inside liquidus and solidus composition bands. The liquidus and solidus bands determine the compositions of the coexisting phases, and the liquidus and solidus lines determine the extent of the two-phase coexistence. (iv) A dramatic increase in solubility is possible. The present paper evaluates the case of Pb-Bi, but the principles should be sufficiently general to hold for other binary alloys as well.

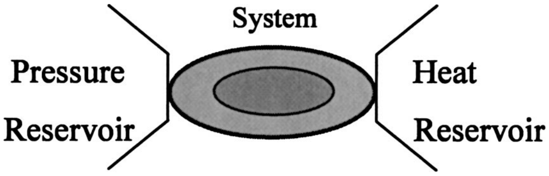

FIG. 10. An isothermal system in contact with constant temperature and a constant pressure reservoirs.

ACKNOWLEDGMENTS

The financial support of the Binational Science Foundation of Israel and the USA is gratefully acknowledged. This work was supported in part through the MRSEC Center for Nanoscopic Materials Design by the National Science Foundation under Award No. DMR-0080016. The authors are grateful to M. Hillert for encouraging conversations.

APPENDIX: THERMODYNAMICAL ANALYSIS

1. The thermodynamical potential

First the thermodynamic potential that is minimized at equilibrium of a system with heterogeneous pressure should be defined.[48,57] Consider such a closed system, in contact with a heat reservoir and a pressure reservoir, interacting with the reservoirs only through the external boundaries of the system (which are considered as flexible and diathermal but impermeable, as illustrated in Fig. 10). Using subscripts "univ," "sys," and "res" for the universe, system, and reservoir, respectively, a general variation in the state of the system changes the internal energy E of the universe by an amount

$$\delta E_{\mathrm{univ}} = \delta E_{\mathrm{sys}} + \delta E^{T}_{\mathrm{res}} + \delta E^{P}_{\mathrm{res}}, \tag{A1}$$

where E^{T}_{res} is the energy of the heat reservoir and E^{P}_{res} is the energy of the pressure reservoir.[57] The state of the heat reservoir is changed (by definition) only by a heat exchange with the system, while the state of the pressure reservoir is changed only by an exchange of mechanical work, and hence

$$\delta E_{\mathrm{univ}} = \delta E_{\mathrm{sys}} + T_{\mathrm{res}} \delta S^{T}_{\mathrm{res}} - P_{\mathrm{res}} \delta V^{P}_{\mathrm{res}} . \tag{A2}$$

The change in volume $\delta V^{P}_{\mathrm{res}}$ of the surrounding isobaric pressure reservoir is also the negative of the change of volume of the system, and $\delta S^{T}_{\mathrm{res}}$ is the change in entropy of the isothermal heat reservoir. According to the second law, the entropy changes obey the equation

$$\delta S_{\mathrm{univ}} = \delta S_{\mathrm{sys}} + \delta S_{\mathrm{res}} \geqslant 0. \tag{A3}$$

Using this inequality,

$$\delta E_{\mathrm{univ}} \geqslant \delta E_{\mathrm{sys}} - T \delta S_{\mathrm{sys}} + P^{\mathrm{ext}} \delta V_{\mathrm{sys}} , \tag{A4}$$

where P^{ext} is the fixed external pressure maintained by the pressure reservoir, T is the isothermal temperature of the system, and V_{sys} is its total volume. At equilibrium the inequality in Eq. (A4) becomes an equality; therefore Eq. (A4) defines a thermodynamic potential ϕ which is minimum at equilibrium ($\delta\phi = 0$):

$$\phi \equiv E_{\mathrm{sys}} - T S_{\mathrm{sys}} + P^{\mathrm{ext}} V_{\mathrm{sys}} = A_{\mathrm{sys}} + P^{\mathrm{ext}} V_{\mathrm{sys}} . \tag{A5}$$

A_{sys} is the Helmholtz free energy of the system and ϕ is minimum at equilibrium in a system with a fixed amount of material, uniform temperature, and a constant *external* pressure but possibly nonuniform internal pressure. The potential ϕ can be viewed as a specialized form of the Gibbs free energy.[58]

Thermodynamic data for binary alloys are available as the Gibbs free energy at 1 atm. However, the pressures in nanoparticles can rise to very high values. In relating the Gibbs function $G(P_{\mathrm{ref}})$ data at low pressure to the Helmholtz function $A(P)$ at the high pressure P, one can show[72] that for incompressible phases $G(P_{\mathrm{ref}} = 0) = A(P)$, and therefore also for the partial quantities of the bulk phases $\mu_i(0) = a_i(P)$.

The potential ϕ of the two-phase system in Fig. 10 or Fig. 2 is

$$\phi = \sum_i n^s_i \mu^s_i(0) + \sum_i n^1_i \mu^1_i(0) + a^{\mathrm{sl}} \Sigma^{\mathrm{sl}} + a^{\mathrm{lg}} \Sigma^{\mathrm{lg}} + P^{\mathrm{ext}} V_{\mathrm{sys}} , \tag{A6}$$

where n is the number of moles of the relevant phase and a is the specific excess Helmholtz free energy of the relevant surface area Σ. The specific surface energy (per unit area) is defined as the excess grand canonical potential of the surface between phases α and β:[59,60]

$$\gamma^{\alpha\beta} = e^{\alpha\beta} - T s^{\alpha\beta} - \sum_i \mu^{\gamma}_i \Gamma^{\alpha\beta}_i = a^{\alpha\beta} - \sum_i \mu^{\gamma}_i \Gamma^{\alpha\beta}_i , \tag{A7}$$

where $e^{\alpha\beta}$ and $s^{\alpha\beta}$ denote the specific excess internal energy and entropy respectively, μ^{γ}_i is the chemical potential associated with the surface adsorbed atoms, and $\Gamma^{\alpha\beta}_i$ is the surface excess quantity of atoms (adsorption) of component i.

By adding and subtracting two $(\Sigma \mu^l_i \Gamma_i)\Sigma$ terms, the surface terms in Eq. (A6) are expressed by the surface energies of Eq. (A7), yielding

$$\begin{aligned}\phi &= \sum_i n^s_i \mu^s_i + \sum_i (n^l_i + \Gamma^{\mathrm{sl}}_i \Sigma^{\mathrm{sl}} + \Gamma^{\mathrm{lg}}_i \Sigma^{\mathrm{lg}}) \mu^l_i \\ &\quad + \left(a^{\mathrm{sl}} - \sum_i \mu^l_i \Gamma^{\mathrm{sl}}_i \right) \Sigma^{\mathrm{sl}} + \left(a^{\mathrm{lg}} - \sum_i \mu^l_i \Gamma^{\mathrm{lg}}_i \right) \Sigma^{\mathrm{lg}} + P^{\mathrm{ext}} V_{\mathrm{sys}} \\ &= \sum_i n^s_i \mu^s_i + \sum_i (n^l_i + \Gamma^{\mathrm{sl}}_i \Sigma^{\mathrm{sl}} + \Gamma^{\mathrm{lg}}_i \Sigma^{\mathrm{lg}}) \mu^l_i \\ &\quad + \gamma^{\mathrm{sl}} \Sigma^{\mathrm{sl}} + \gamma^{\mathrm{lg}} \Sigma^{\mathrm{lg}} + P^{\mathrm{ext}} V_{\mathrm{sys}} .\end{aligned} \tag{A8}$$

All the chemical potentials in this equation are evaluated at zero pressure; the chemical potentials in both the inner and outer boundaries of the liquid have been taken as those of the liquid. In practice, $\Delta\phi$, the difference between the potential ϕ for the two-phase particle and a reference state, chosen to be the solid particle before it melts, will be calculated. Plotting $\Delta\phi$ will permit the identification of the stable states of the system, namely, the states of the minimum in $\Delta\phi$.

2. The equilibrium conditions

An alternative way to identify the stable states of the nanoparticle is to find the minimum of $\Delta\phi$ analytically. To this end, the differential of ϕ given in Eq. (A8) is evaluated and equated to zero:

$$\begin{aligned} d\phi &= \sum_i \mu^s_i dn^s_i + \sum_i n^s_i d\mu^s_i + \sum_i \mu^l_i d(n^l_i + \Sigma^{\mathrm{sl}} \Gamma^{\mathrm{sl}}_i + \Sigma^{\mathrm{lg}} \Gamma^{\mathrm{lg}}_i) \\ &\quad + \sum_i n^l_i d\mu^l_i + \sum_i \Sigma^{\mathrm{sl}} \Gamma^{\mathrm{sl}}_i d\mu^l_i + \sum_i \Sigma^{\mathrm{lg}} \Gamma^{\mathrm{lg}}_i d\mu^l_i + \gamma^{\mathrm{sl}} d\Sigma^{\mathrm{sl}} \\ &\quad + \Sigma^{\mathrm{sl}} d\gamma^{\mathrm{sl}} + \gamma^{\mathrm{lg}} d\Sigma^{\mathrm{lg}} + \Sigma^{\mathrm{gl}} d\gamma^{\mathrm{gl}} + P^{\mathrm{ext}} dV_{\mathrm{sys}} = 0. \end{aligned} \tag{A9}$$

To simplify this equation, the Gibbs-Duhem relations are applied. For the solid and liquid phases of volumes V^s and V^l at constant temperature,

$$V^s dP^s - \sum_i n^s_i d\mu^s_i = 0, \tag{A10a}$$

$$V^l dP^l - \sum_i n^l_i d\mu^l_i = 0. \tag{A10b}$$

For the bulk solid and liquid at zero pressure the first term in each equation vanishes. For the surface phases the Gibbs-Duhem relation at constant temperature, generalized to include the effect of the surface stress f^{ab}, is[61]

$$(\gamma^{\mathrm{sl}} - f^{\mathrm{sl}}) d\Sigma^{\mathrm{sl}}_e + \sum_i \Sigma^{\mathrm{sl}} \Gamma^{\mathrm{sl}}_i d\mu^{\gamma}_i + \Sigma^{\mathrm{sl}} d\gamma^{\mathrm{sl}} = 0, \tag{A10c}$$

$$(\gamma^{\mathrm{lg}} - f^{\mathrm{lg}}) d\Sigma^{\mathrm{lg}}_e + \sum_i \Sigma^{\mathrm{lg}} \Gamma^{\mathrm{lg}}_i d\mu^{\gamma}_i + \Sigma^{\mathrm{lg}} d\gamma^{\mathrm{lg}} = 0. \tag{A10d}$$

The elastic deformation $d\Sigma_e$ of the surface is taken to be zero for the accretive variation at the solid-liquid interface because of the assumption of incompressible phases. For liquids, γ and f are identical,[62] so for both solid and liquid phases the first term is zero. The second terms in Eqs. (A10c) and (A10d) include the variation of γ with the composition and pressure, to be discussed in the next section. As in Eq. (A8) we take $d\mu^{\gamma}$ in Eqs. (A10c) and (A10d) to be $d\mu^{l}$ and substitute Eqs. (A10) into Eq. (A9) to yield

$$d\phi=\sum_i \mu_i^s dn_i^s+\sum_i \mu_i^l d(n_i^t-n_i^s)+\gamma^{\mathrm{sl}}d\Sigma^{\mathrm{sl}}+\gamma^{\mathrm{lg}}d\Sigma^{\mathrm{lg}}+P^{\mathrm{ext}}dV_{\mathrm{sys}}=0, \tag{A11}$$

where the following mass conservation condition for each constituent has been used, denoting the atomic fraction of each component by X_i^s and X_i^l and the overall composition by $X_{0,i}$:

$$n_i^t=X_{0,i}n^t=X_i^s n^s+X_i^l n^l+\Sigma^{\mathrm{sl}}\Gamma_i^{\mathrm{sl}}+\Sigma^{\mathrm{lg}}\Gamma_i^{\mathrm{lg}}. \tag{A12}$$

For a two-component system, two partial derivatives of ϕ with respect to dn_i^s are obtained from Eq. (A11):

$$\frac{d\phi}{dn_i^s}=\mu_i^s-\mu_i^l+\gamma^{\mathrm{sl}}\frac{d\Sigma^{\mathrm{sl}}}{dn_i^s}+\gamma^{\mathrm{lg}}\frac{d\Sigma^{\mathrm{lg}}}{dn_i^s}=0, \tag{A13}$$

where the derivative of the term $P^{\mathrm{ext}}dV_{\mathrm{sys}}$ is neglected in view of the small magnitude of the external pressure.

The remaining derivatives are evaluated using the chain rule:

$$\frac{d\Sigma^{\mathrm{sl}}}{dn_i^s}=\frac{d\Sigma^{\mathrm{sl}}}{dV^s}\frac{dV^s}{dn_i^s}=\frac{2}{r_s}\overline{V_i^s},$$

$$\frac{d\Sigma^{\mathrm{lg}}}{dn_i^s}=\frac{d\Sigma^{\mathrm{lg}}}{dV^{\mathrm{tot}}}\frac{dV^{\mathrm{tot}}}{dn_i^s}=\frac{2}{R}(\overline{V_i^s}-\overline{V_i^l}), \tag{A14}$$

for a spherical particle with a solid core of radius r_s and a liquid sheath of radius R (Fig. 2), where $\overline{V_i^s}$ and V_i^l are the specific volumes of the component i in the solid and liquid, respectively. Thus Eqs. (A13) reduce to

$$\mu_A^s(0)-\mu_A^l(0)=-\frac{2\gamma^{\mathrm{sl}}}{r_s}\overline{V_A^s}-\frac{2\gamma^{\mathrm{lg}}}{R}(\overline{V_A^s}-\overline{V_A^l}),$$

$$\mu_B^s(0)-\mu_B^l(0)=-\frac{2\gamma^{\mathrm{sl}}}{r_s}\overline{V_B^s}-\frac{2\gamma^{\mathrm{lg}}}{R}(\overline{V_B^s}-\overline{V_B^l}). \tag{A15}$$

Equation (A15) implies a shift of the states of equilibrium of a solid and a liquid in the shape of a small particle relative to the same alloy in the bulk form, where equilibrium satisfies

$$\mu_i^s(0)-\mu_i^l(0)=0. \tag{A16}$$

The notation $\mu(0)$ serves to emphasis that the chemical potential is measured at ambient pressure. For pure materials slightly deviated from the bulk melting temperature, $\mu^s(0)-\mu^l(0)=\Delta H_{\mathrm{melt}}(T_m-T)/T_m$. Substitution in Eqs. (A15) yields approximately Eq. (1).

Equation (A15) was derived by Hanszen[35] and conforms with several experimental results on the melting temperatures of pure metals (as mentioned in the Introduction). Although Eqs. (A15) do not show explicitly the effect of adsorption, their practical solution requires application of the mass conservation equation (A12), where the adsorption is taken into account. The difference between the chemical potentials at the actual pressures prevailing in the nanoparticle is also implicit in Eqs. (A15). This can be seen by adding $p^s\overline{V_i^s}-p^l\overline{V_i^l}$ to both sides of Eq. (A15) and adding and subtracting $p^l\overline{V_i^s}$ to the right-hand side, yielding

$$\begin{aligned}[\mu_i^s(0)+p^s\overline{V_i^s}]-[\mu_i^l(0)+p^l\overline{V_i^l}]&=(p^s-p^l)\overline{V_i^s}-\frac{2\gamma^{\mathrm{sl}}}{r_s}\overline{V_i^s}+p^l(\overline{V_i^s}-\overline{V_i^l})\\&\quad-\frac{2\gamma^{\mathrm{lg}}}{R}(\overline{V_i^s}-\overline{V_i^l}).\end{aligned} \tag{A17}$$

For an isotropic sphere $p^s-p^l=2f^{\mathrm{sl}}/r_s$, where f^{sl} is the surface stress of the solid-liquid interface and, neglecting the pressure of the surrounding gas, $p^l=2\gamma^{\mathrm{lg}}/R$ ($\gamma=f$ for liquids). Substitution of these relations reduces Eq. (A17) to

$$\mu_i^s(p^s)-\mu_i^l(p^l)=\frac{2(f^{\mathrm{sl}}-\gamma^{\mathrm{sl}})}{r_s}\overline{V_i^s}. \tag{A18}$$

This discontinuity of the chemical potential was found by Gibbs[63] for a particle of a pure material embedded in a large quantity of fluid and was extended by Cahn[64] to alloy particles. It contradicts other conventions,[41,65–69] according to which the pressure jump is $2\gamma/r$ but the chemical potential is continuous across curved boundaries. The solution to Eq. (A15) or Eq. (A18) yields the special behavior of the melting of nanoparticle alloys detailed in Sec. V, which conforms with the experimental observations described in Sec. III.

---

[1] Y. Xi, Z. L. Ying, B. X. Bing, L. Peng, Acta Phys. Sin. **51**, 1628 (2002); X. Wang and H. Chen, Mater. Chem. Phys. **75**, 2 (2002).

[2] Z. Yue, J. Zhou, X. Wang, Z. Gui, and L. Li, J. Eur. Ceram. Soc. **23**, 189 (2003).

[3] *Semiconductor Quantum Dots, Physics, Spectroscopy and Applications*, edited by Y. Masumoto and T. Takagahara (Springer, Stuttgart, 2002).

[4] Z. Zhu, Y. Gao, X. Z. Che, Y. Q. Yang, and C. Y. Chung, J. Alloys Compd. **330-332**, 708 (2002).

[5] G. L. Allen and W. A. Jesser, J. Cryst. Growth **70**, 546 (1984); N. Mattern, U. Kuhn, and J. Eckert, *Science of Metastable and Nanocrystalline Alloys*, edited by A. R. Dinesen, M. Eldrup, D. Juul Jensen, S. Linderoth, T. B. Pedersen, N. H. Pryds, A. Schroder Pedersen, and J. A. Wert (Riso National Laboratory, Roskilde, Denmark, 2001), p. 323.

[6] J. Said, M. Matsushita, and A. Inoue, Mater. Trans., JIM **42**, 1103 (2001); A. Jianu, M. Bunescu, R. Nicula, Ch. Lathe, G. Holzhuter, and E. Burkel, in *Science of Metastable and Nano-*

crystalline Alloys (Ref. 5), pp. 35 and 271.

[7] J. A. Ascencio, M. Perez, and M. Jose-Yacaman, Surf. Sci. **447**, 73 (2000).

[8] S. Tsunekawa, R. Silvamohan, S. Ito, A. Kasuya, and T. Fukuda, Nanostruct. Mater. **11**, 141 (1999); T. Volkmann, J. Gao, B. Wei, and D. M. Herlach, in *Science of Metastable and Nanocrystalline Alloys* (Ref. 5), p. 417.

[9] K. Lu, Mater. Sci. Eng., R. **16**, 161 (1996).

[10] H. Konrad, J. Weissmuller, R. Birringer, C. Karmonik, and H. Gleiter, Phys. Rev. B **58**, 2142 (1998).

[11] H. Gleiter, Nanostruct. Mater. **1**, 48 (2000).

[12] D. Poondi and J. Singh, J. Mater. Sci. **35**, 2467 (2000).

[13] S. Ramos de Debiaggi, J. M. Campillo, and A. Caro, J. Mater. Res. **14**, 2849 (1999); I. Brodova, D. Bashlykov, A. Manukhin, I. Shirinkina, V. Stolyarov, and E. Soshnikova, in *Science of Metastable and Nanocrystalline Alloys* (Ref. 5), p. 223.

[14] J. Weissmuller and C. Lemier, Philos. Mag. Lett. **80**, 411 (2000).

[15] S. S. Flaschen, J. Am. Chem. Soc. **77**, 6194 (1955).

[16] G. Skandan, C. M. Foster, H. Frase, M. N. Ali, J. C. Parker, and H. Hahn, Nanostruct. Mater. **1**, 313 (1992).

[17] R. C. Garvie, J. Phys. Chem. **82**, 218 (1978).

[18] T. Chraska, A. H. King, C. C. Berndt, and J. Karthikeyan, in *Phase Transformations and Systems Driven Far from Equilibrium*, edited by E. Ma, P. Bellon, M. Atzmon, and R. Trivedi, MRS Symposia Proceedings No. 481 (Materials Research Society, Pittsburgh, 1998), 613.

[19] J. M. McHale, A. Auroux, A. J. Perrotta, and A. Navrotsky, Science **277**, 788 (1997).

[20] H. Zhang and J. F. Banfield, in *Phase Transformations and Systems Driven Far from Equilibrium* (Ref. 18), p. 619.

[21] J. Weissmuller, Mater. Sci. Eng., A **179/180**, 102 (1994).

[22] M. Takagi, J. Phys. Soc. Jpn. **9**, 359 (1954).

[23] C. J. Coombes, J. Phys. F **2**, 441 (1972).

[24] R. P. Berman and A. E. Curzon, Can. J. Phys. **52**, 923 (1974).

[25] V. P. Skripov, V. P. Koverda, and V. N. Skokov, Phys. Status Solidi A **66**, 109 (1981).

[26] M. Blackman and A. E. Curzon, *Structure and Properties of Thin Films* (Wiley, New York, 1959), p. 217.

[27] C. R. M. Wronski, Br. J. Appl. Phys. **18**, 1731 (1967).

[28] M. S. Rahman, Micron **13**, 273 (1982).

[29] G. L. Allen, Ph.D. dissertation, University of Virginia, 1985.

[30] G. L. Gile, MS dissertation, University of Virginia, 1982.

[31] S. J. Peppiatt and J. R. Sambles, Proc. R. Soc. London, Ser. A **345**, 387 (1975); **345**, 401 (1975).

[32] N. T. Gladkich, R. Niredermayer and K. Spiegel, Phys. Status Solidi **15**, 181 (1966).

[33] P. Buffat and J. P. Borel, Phys. Rev. A **13**, 2287 (1976).

[34] A. N. Goldstein, C. M. Echer, and A. P. Alivisatos, Science **256**, 1425 (1992).

[35] K. J. Hanszen, Z. Phys. **157**, 523 (1960).

[36] P. R. Couchman and W. A. Jesser, Nature (London) **269**, 481 (1977).

[37] M. Hasegawa, K. Hoshino, and M. Watabe, J. Phys. F: Met. Phys. **10**, 619 (1980).

[38] L. S. Palatnik and B. T. Boiko, Phys. Met. Metallogr. **11**, 119 (1961).

[39] R. P. Berman, Ph.D. dissertation, Simon Fraser University, 1975.

[40] W. A. Jesser, G. J. Shiflet, G. L. Allen, and J. L. Crawford, Mater. Res. Innovations **2**, 211 (1999).

[41] T. Tanaka and S. Hara, Z. Metallkd. **92**, 467 (2001); **92**, 1236 (2001).

[42] N. Saunders and A. P. Midownik, *CALPHAD: A Comprehensive Guide* (Pergamon, London, 1998).

[43] J. R. Wilson, Metall. Rev. **10**, 381 (1965).

[44] L. Granasy and M. Tegze, Mater. Sci. Forum **77**, 243 (1991).

[45] T. Tanaka, K. Hack, and S. Hara, MRS Bull. **24(4)**, 45 (1999).

[46] R. A. Angal and D. L. Roy, Z. Metallkd. **73**, 428 (1982).

[47] T. Utigard and J. M. Toguri, Metall. Trans. B **18**, 695 (1987).

[48] R. Defay, I. Prigogine, and A. Bellemans, *Surface Tension and Adsorption* (Wiley, New York, 1966), Chap. 1.

[49] S. M. Kaufman and T. J. Whalen, Acta Metall. **13**, 797 (1965).

[50] F. O. Koeing, J. Chem. Phys. **18**, 440 (1950).

[51] O. J. Kleppa, M. Kaplan, and C. E. Thalmayer, J. Phys. Chem. **64**, 843 (1961).

[52] B. Pluis, A. W. Denier van der Gon, J. F. van der Veen, and A. J. Riemersma, Surf. Sci. **239**, 265 (1990).

[53] T. Utigard, Z. Metallkd. **84**, 792 (1993).

[54] S. Kristyan and J. Giber, Surf. Sci. **201**, L532 (1988).

[55] M. E. Glicksman and C. L. Vold, Acta Metall. **17**, 1 (1969).

[56] L. E. Murr, *Interfacial Phenomena in Metals and Alloys* (Addison-Wesley, Reading, MA, 1975), Chaps. 3 and 4.

[57] H. B. Callen, *Thermodynamics* (Wiley, New York, 1985).

[58] M. Hillert, *Phase Equilibria, Phase Diagrams and Phase Transformations: Their Thermodynamic Basis* (Cambridge University Press, Cambridge, 1998), Chaps. 1 and 7.

[59] C. Herring, in *Structure and Properties of Solid Surfaces*, edited by R. Gomer and C. S. Smith (University of Chicago Press, Chicago, 1953) p. 5.

[60] R. G. Linford, in *Solid State Surface Science*, edited by M. Green, vol. **2**, p. 1.

[61] P. R. Couchman, W. A. Jesser, and D. H. Everett, J. Colloid Interface Sci. **52**, 410 (1975).

[62] R. Shuttleworth, Proc. Phys. Soc. London **A63**, 444 (1950).

[63] J. W. Gibbs, *The Collected Works of W. J. Gibbs* (Longmans, Green, New York, 1928), pp. 194, 229, and 317.

[64] J. W. Cahn, Acta Metall. **28**, 1333 (1980).

[65] W. W. Mullins, J. Chem. Phys. **81**, 1436 (1984).

[66] W. W. Mullins and R. F. Sekerka, J. Chem. Phys. **82**, 5192 (1985).

[67] P. H. Leo and R. F. Sekerka, Acta Metall. **37**, 3119 (1989).

[68] J. I. D. Alexander and W. C. Johnson, J. Appl. Phys. **58**, 816 (1985).

[69] P. W. Voorhees and W. C. Johnson, J. Chem. Phys. **90**, 2793 (1989).

[70] In Figs. 5 and 6 two areas are absent due to restrictions of material conservation. The first is beyond the hyperbolic border at high bismuth compositions and liquid fractions Beyond this border the amount of bismuth in the liquid is larger than the amount present in the entire particle. The second excluded region has a border lying beyond the inclined line at low liquid fractions. This region is excluded because the amount of bismuth in the liquid and the amount required by the equation for the adsorption to the l-g surface exceeds the amount of bismuth in the entire particle.

[71] A. S. Shirinyan and A. M. Gusak, Philos. Mag. **84**, 579 (2004).

[72] By definition $G=A+PV$, and hence at zero pressure $G(0)=A(0)$. The change of the Helmholtz free energy of an isothermal pressurizing is $dA=P\,dV$, which is zero for an incompressible material. Hence $A(P)=A(0)$ and therefore $A(P)=G(0)$. For real solid and liquid materials this is a good approximation, which we use here.